EXOSC10 mediated RNA degradation sculpts the transcriptome during oocyte growth-to-maturation transition

Di Wu*, Cameron Palmer and Jurrien Dean
Laboratory of Cellular and Developmental Biology, NIDDK,
National Institutes of Health, Bethesda, Maryland 20892
*corresponding author: di.wu2@nih.gov

Abstract

Disorders of ovulation account for 40% of female infertility to which improper oocyte maturation contributes significantly. During mammalian oogenesis, oocytes accumulate substantial amounts of RNA in the growth phase, the majority of which is degraded during subsequent maturation. The growth-to-maturation transition begins with nuclear envelope breakdown, which is designated germinal vesicle breakdown (GVBD) in oocytes. A successful growth-to-maturation transition is essential for subsequent ovulation, fertilization and embryogenesis. Previous studies documented important characteristics of this transition, including cAMP-PKA signaling, SUMOylation and CDK phosphorylation. However, the concomitant changes in the oocyte transcriptome during GVBD remained unclear. Here, we report that an RNA exosome associated RNase, EXOSC10, degrades poly(A) RNA to facilitate the oocyte growth-to-maturation transition. We establish an oocyte-specific conditional knockout of *Exosc10* in mice using CRISPR/Cas9 and document female subfertility. We further determine that oocyte growth is not affected, but maturation is delayed or blocked with failed GVBD in EXOSC10 depleted oocytes. We performed single oocyte RNA-seq at GV, GVBD and MII stages and employed ERCC spike-in normalization to compare transcriptomes among these stages. scRNA-seq documents dysregulated transcriptomes in mutant oocytes, and many up regulated RNAs that encode proteins important for protein trafficking, cell cycle and RNA metabolism. We find impaired early to late endosome maturation and overall disruption of endoplasmic reticulum and lysosomes, which confirm defects in the endomembrane system. In addition, CDK1 phosphorylation fails to change from inhibitory to active, which blocked lamina phosphorylation and disassembly in the mutant oocytes. Collectively, we propose that EXOSC10 promotes the growth-to-maturation transition in oocytes by degrading growth-phase factors and sculpting the transcriptome to the maturation phase of oogenesis.

Introduction

Improper oocyte maturation directly causes ovulatory disorders and leads to female infertility (Jose-Miller et al., 2007; Macklon et al., 2002). Maturing oocytes dramatically alter their transcriptome due to active RNA degradation in the absence of transcription. A growing body of work documents that coordinated sequestration, deadenylation, translation and degradation collectively regulate RNA metabolism during oocyte maturation. A dysregulated transcriptome can impair oogenesis and post-fertilization embryogenesis (Burns et al., 2003; Metchat et al., 2009; Wasielak et al., 2016; Yu et al., 2016).

For historic reasons, the oocyte nucleus is referred to as the germinal vesicle (GV). After their growth phase, GV-intact oocytes remain quiescent in pre-ovulatory follicles until induced to mature by luteinizing hormone. Critical events in the transition from growth to maturation include chromatin condensation, termination of transcription and nuclear envelope breakdown (GVBD). The first two are directly coupled and are dominated by an increase of repressive histone modifications including H3K9 methylation that sculpts the oocyte chromatin (Dumdie et al., 2018; Kageyama et al., 2007). The third event, GVBD, requires precise coordination of the

meiotic cell cycle and membrane trafficking. Meiotic cell cycle control is determined by the cyclin B/CDK1 activity through complex signaling pathways including cAMP-PKA and PKB/Akt (Kishimoto, 2018). High levels of cAMP cause CDK1 inhibitory phosphorylation that favors GV arrest. Conversely, decreases of cAMP activate CDK1 to form the functional cyclin B/CDK1 complex that induces GVBD. The membrane trafficking machinery involves endomembrane components. For example, an exchange apparatus of ER-NE (endoplasmic reticulum - nuclear envelope) has been reported to facilitate NE formation post mitosis by reorganizing membrane structure around chromatin (Anderson and Hetzer, 2008). The COPI-coated vesicles that normally traffic from the Golgi to ER also promote GVBD upon recruitment by nucleoporin Nup153 (Liu et al., 2003). However, the molecular basis of the observed coordination of transcriptome sculpting with GVBD remains undetermined.

The RNA exosome is a highly conserved complex that degrades or processes cellular RNAs from the 3' end. RNA exosome-related genetic mutations have been identified in a wide range of diseases, including diarrhea of infancy, neurodegenerative disorders and multiple myeloma (Hartley et al., 2010; Rudnik-Schöneborn et al., 2013; Weissbach et al., 2015). The association of the core complex with DIS3, DIS3L or EXOSC10 RNases provides the required enzymatic activity. EXOSC10 is a nuclear RNase, the absence of which causes RNA processing defects in yeast (Carneiro et al., 2007) and increased sensitivity to DNA damage in fly and human cells (Domingo-Prim et al., 2019; Rolfsmeier et al., 2011). EXOSC10 has been documented to promote mRNA turnover (van Dijk et al., 2007), 3' pre-rRNA processing (Knight et al., 2016) and long noncoding/enhancer RNA degradation (Pefanis et al., 2015). It also has been reported to control the onset of spermatogenesis in male germ cells (Jamin et al., 2017). However, whether EXOSC10 is essential for oogenesis has remained unclear. Published datasets document that *Exosc10* transcript are highly abundant in mouse oocytes and early embryos (Yu et al., 2016), raising the possibility of its participation in maternal RNA metabolism.

In the current study to evaluate EXOSC10 function in the oogenesis, we established oocyte-specific conditional *Exosc10* knockout (cKO) mice. cKO females had decreased fecundity associated with defects in GVBD and delayed oocyte maturation. Using single oocyte RNA-seq and ERCC spike-in normalization, we identified dysregulated transcripts involved in endomembrane disfunction and abnormal CDK1 phosphorylation.

Materials and Methods

Mice

Mice were maintained in compliance with the guidelines of the Animal Care and Use Committee of the National Institutes of Health under a Division of Intramural Research, NIDDK-approved animal study protocol.

Generation of *Exosc10* floxed allele by CRISPR/Cas9

Two guide RNAs (gRNA, 50 ng/μl), two homology-directed repair (HDR, 100 ng/μl) templates and *Cas9* cRNA (100 ng/μl) were microinjected into 1-cell mouse embryos. The two gRNA sequences are: 5'tcagtggagacctgcgatct3' (left loxP) and 5'gaaattctgatgtctagcgg3' (right loxP). Each gRNA was *in vitro* transcribed from a double stranded (ds) DNA template by MEGAshortscript™ T7 Transcription Kit (AM1354) and purified by MEGAclear Transcription Clean-Up Kit (AM1908). The dsDNA templates for sgRNAs were initially synthesized as single stranded (ss) DNA from Integrated DNA Technologies and amplified by primers 5'GATCCCTAATACGACTCACTATAG3' and 5' AAAAAAAGCACCGACTCGGTGCCAC3' into double stranded DNA:
5'gatccctaatacgactcactataggtcagtggagacctgcgatctgttttagagctagaaatagcaagttaaaataaggctagtccgt

tatcaacttgaaaaagtggcaccgagtcggtgctttttt3' and
5'gatccctaatacgactcactatagggaaattctgatgtctagcgggttttagagctagaaatagcaagttaaaataaggctagtccgtt atcaacttgaaaaagtggcaccgagtcggtgctttttt3'.

The two HDR templates for each edited locus were synthesized as ssDNA from IDT:
5'gagagagcacgtatggctcttgcagaggactggtactctaccccagcacccatgttaggtgggtcacaactgcttgtaactccagct ccaagaGCGGCCGCATAACTTCGTATAATGTATGCTATACGAAGTTATtcgcaggtctccactgacactg gcactcaggagcacgt3' (left loxP) and
5'actcacactgtagaccagtctggcctcaaactcacaaagatccacctgcctctgcctcctaagtgctggggttaaatgggtactctac caccgGAATTCATAACTTCGTATAGCATACATTATACGAAGTTATctagacatcagaatttctaaatataaaa aggagaatg3' (right loxP).

After linearization by PmeI, plasmid #42251 (Addgene) was used as a template to transcribe *Cas9* cRNA *in vitro* by mMESSAGE mMACHINE™ T7 ULTRA Transcription Kit (AM1345). The synthesized cRNA was purified by MEGAclear Transcription Clean-Up Kit (AM1908).

For mouse embryo microinjections, hormonally stimulated $B6D2_{F1}$ female mice were mated to $B6D2_{F1}$ males. 1-cell zygotes were flushed from oviducts into M2 medium (#M2114, CytoSpring) and microinjected with the mixed components for gene-editing with CRISPR/Cas9. The injected embryos were cultured in KSOM (#K0113, CytoSpring) at 37 °C with 5% CO_2 for 24 hr. 2-cell embryos were transferred into the oviducts of 0.5-day post coitus pseudopregnant ICR females.

To obtain *Exosc10* oocyte-specific conditional KO mice (cKO), *Exosc10* floxed mice were crossed to *Zp3-cre* mice. The genotyping primers for *Exosc10* floxed allele and deletion allele are as follows:

left loxP: 5'atgagtcgggtaatgcagtac and 5'tgtgtgaggatgttgtgagc3';

right loxP: 5'ccgactctgacattgagtgg3' and 5'gcctctttcccacagttccag3';

Deletion allele: 5'atgagtcgggtaatgcagtac and 5'gcctctttcccacagttccag3;

Cre: 5'gcggtctggcagtaaaaactatc3' and 5'gtgaaacagcattgctgtcactt3'.

Oocyte collection and culture

Ovaries were dissected from female mice (6-10 w/o) into M2 medium plus Milrinone (2.5 μM). The ovaries were pierced mechanically by 30-gauge-needles to release oocytes into M2 (Milrinone) medium. Only fully-grown oocytes (GV oocytes) detaching easily from the granulosa cells were collected for further experiments. For oocyte *ex vivo* maturation, GV oocytes were washed (10X) with M2 medium without Milrinone and cultured in M2 at 37 °C with 5% CO_2. The GVBD/GV ratio was determined at GV+3hr and meiosis II progression rate was evaluated at 14 hr.

cRNA *in vitro* transcription and microinjection

The *Exosc10* coding sequence was inserted into plasmid #44118 (Addgene) to form in-frame fusion with mVenus. Simultaneously a T7 promoter (TAATACGACTCACTATAGGG) was inserted into the 5' end of the *Exosc10* coding sequence. The plasmid was linearized by XbaI, purified and *in vitro* transcribed by mMESSAGE mMACHINE™ T7 ULTRA Transcription Kit (ThermoFisher AM1345). The cRNAs were purified by MEGAclear Transcription Clean-Up Kit (AM1908) and diluted into proper concentration (500 ng/μl unless otherwise stated) for microinjection.

Immunofluorescence and confocal microscopy

Ex vivo cultured oocytes or embryos were fixed by 2 % paraformaldehyde (#50-980-492 Fisher Scientific, diluted in PBS containing 0.5% Triton X-100) at 37 °C for 30 min. After fixation,

oocytes were washed with PBVT (PBS, 3mg/ml Polyvinylpyrrolidone-40 and 1% Tween-20), and permeabilized with 0.5% Triton X-100 in PBS for 30 min at room temperature. Oocytes were blocked by 5% normal goat serum in PBVT for 1 hr at room temperature followed by primary antibody incubation overnight at 4 °C. On the second day, the oocytes were washed (4X, 15 min) with PBVT and incubated into fluorescence conjugated secondary antibody overnight at 4 °C. On the third day, after washing by PBVT (4X, 15 min), oocytes were stained with DAPI and mounted with PBS for confocal microscopic imaging (LSM 780; Carl Zeiss).

Source and dilution of antibodies, staining reagents and live staining dyes

Anti-GM130 (1:200, BD Transduction Laboratories 610823); LysoTracker™ Green DND-26 (1:1000, ThermoFisher L7526); LysoTracker™ Blue DND-22 (1:1000, ThermoFisher L7525); ER tracker red (1:1000, Invitrogen E34250); anti-lamin B1 (B-10) (1:200, Santa Cruz sc-374015); anti-αtubulin (1:200, Sigma T5168); anti-lamin A/C (4C11) (1:200, CST 4777T); anti-phospholamin A/C (Ser22) (1:200, CST 2026); anti-rab5 [EPR21801] (1:500, Abcam ab218624); anti-phosphoCDK1 (Thr14, Tyr15) (17H29L7) (1:200, ThermoFisher 701808); anti-cAMP (1:200, RD # MAB2146); anti-pericentrin (1:2000, Abcam #ab4448); anti-γtubulin (1:500, Abcam ab11316); goat anti-rabbit IgG (H+L) Cross-Adsorbed Secondary Antibody, Alexa Fluor 546 (1:500, Invitrogen A-11010); goat anti-mouse IgG (H+L) Cross-Adsorbed Secondary Antibody, Alexa Fluor 647 (1:500, Invitrogen A-21235). DAPI (Sigma D9542-1MG); goat serum (Sigma G9023-10ML); Tween-20 (Sigma P1379-25ML).

Ovary histology

Ovaries were dissected from female mice of desired ages into PBS buffer. After removing the surrounding lipid and tissue, the ovaries were fixed in newly prepared 2.5% glutaraldehyde and 2.5% paraformaldehyde in 0.083 M sodium cacodylate buffer (pH 7.2) for 3-5 hr at 4 °C. Ovaries were washed with 0.1M sodium cacodylate buffer (pH 7.2) and kept at 4 °C overnight. Finally, the ovaries were transferred into 70% ethanol and stocked for more than 1 day at 4 °C. The sectioning (2 μm, every 20th section), periodic acid–Schiff (PAS) staining and mounting were performed by American HistoLab. The imaging of ovary histology was performed on a Nikon ECLIPSE Ti microscope using a 20x objective.

RNA FISH of oligo(dT) probe

FISH assays were performed in U-bottom 96-well plates. Oocytes at desired stages were fixed with 2 % paraformaldehyde (#50-980-492 Fisher Scientific, diluted in PBS containing 0.5% Triton X-100) at 37 °C for 30 min. Oocytes were dehydrated stepwise at room temperature using 25%, 50%, 75%, 100% (methanol: PBS volume) and washed (3X) with 100% methanol. After -20 °C treatment >1 hr, the oocytes were rehydrated into PBT (PBS-0.1% Tween-20) through 75%, 50%, 25%, 0% (methanol: PBT volume) steps. Oocytes then were washed (3X) with PBT, treated with 0.5% SDS for 30 min at room temperature and re-washed (3X) with PBT. Oocytes were washed (2X) with newly prepared FISH Wash Buffer (10% formamide, 2x SSC, 1/1000 Tween-20 in nuclease-free water), transferred into hybridization buffer (10% formamide, 2x SSC, 10% dextran sulfate in nuclease-free water) and incubated at 37 °C for 2 hr. The oocytes then were incubated with probe-containing hybridization buffer for 16 hr at 37 °C. On the second day, oocytes were incubated sequentially with hybridization buffer (30 min, 37 °C), FISH Wash Buffer (1X, 5 min; 4X, 20 min at 37 °C), and FISH wash buffer (1X, 20 min) at room temperature. Oocytes were further washed (2X) with PBT at room temperature, mounted onto ProLong™ Diamond Antifade Mountant (P36970) and imaged by confocal microscopy (LSM 780; Carl Zeiss).

Single oocyte RNA-seq library preparation

Single oocyte RNA-seq libraries were prepared according to a published single-cell RNA seq pipeline with minor modifications (Macaulay et al., 2016). Briefly, oocytes at desired stages were collected individually into 2.5 μl RLT Plus (Qiagen) and stored at -80 °C until all samples were acquired. In the beginning of RNA purification, ERCC RNA spike-in mix (ThermoFisher 4456740) was diluted 10^5 fold, and 1 μl of the diluted ERCC mix was added to each sample. Poly(A) RNA was isolated by oligo (dT) beads, reverse transcribed, amplified and purified. A preliminary sequencing was performed with different amplification cycles (10, 12, 14, 16, 18) and different portions of oocytes as initial material (1/8, 1/4, 1/2, 1) to test the linear range of amplification. 14 cycles was chosen as the best condition based on the regression analysis of ERCC. The purified cDNAs were analyzed by Bioanalyzer 2100 to confirm successful amplification and quality. Qualified cDNAs were used to construct sequencing libraries by Nextera DNA Sample Preparation Kits. The generated 72 sequencing libraries were evaluated by Bioanalyzer 2100 and pooled into 6 groups for purification. The sequencing was performed by NIDDK Genomic Core Facility.

RNA-seq analysis based on ERCC RNA spike-in mix.

Raw sequence reads were trimmed with cutadapt 1.18 to remove adapters while performing light quality trimming with parameters "-a CTGTCTCTTATA -q 20 --minimum-length=25." Sequencing library quality was assessed with fastqc v0.11.8 with default parameters. The presence of common sequencing contaminants was evaluated with fastq screen v0.13.0 with parameters "--subset 100000 --aligner bowtie2." Trimmed reads were mapped to the Mus musculus mm10 reference genome plus ERCC.fasta using hisat2 2.1.0 with default parameters. Multi-mapping reads were filtered using samtools 1.9. Uniquely aligned reads were then mapped to gene features using subread featureCounts v1.6.2 as an unstranded library with default parameters. A gene/ERCC count was considered valid when present in at least 5 reads in at least 2 libraries. The oocyte libraries were normalized by ERCC counts by defining controlGenes in estimating sizeFactors. Differential expression between groups of samples was tested using R version 3.5.1 (2018-07-02) with DESeq2 1.20.0. Transcript quantification was performed with salmon 0.11.3 with parameters "--gcBias --libType A --seqBias --threads 1."

Quantitative RT-PCR

Single oocytes were collected individually for poly(A) RNA enrichment, purification, reverse-transcription and amplification following a similar pipeline as single oocyte RNA-seq protocol. The purified cDNA was directly used as templates and the qRT-PCR was performed by iTaq Universal SYBR Green Supermix (Bio-Rad #1725121) and QuantStudio 6 Flex Real-Time PCR System. The primers for *Exosc10* and *Gapdh* are:

Exosc10 primer 1: 5'ccgactctgacattgagtgg3' and 5'gcctctttcccacagttccag3';

Exosc10 primer 2: 5'ATCCCCCAGGGAAAGACTTC3' and 5'GTCCGACTTTCCAACAGCAA3';

G*apdh*: 5'TGCACCACCAACTGCTTAGC3' and 5'GGCATGGACTGTGGTCATGAG3'.

Electron Microscopy. Mouse GV oocytes were collected from unstimulated ovaries, washed (2X) with PBS, and fixed by newly prepared 2.0% glutaraldehyde, 2.5% PFA in 0.1M cacodylate buffer (pH 7.4) for 10 min at room temperature followed by 2 hr on ice. Fixed oocytes were washed (3X) with 0.1M cacodylate buffer. Oocytes were embedded in 1% agarose (Sigma A2576) and stored in 0.1M cacodylate buffer overnight at 4°C. Following sample preparation for transmission electron microscopy, sectioning and imaging were performed by NIBIB Electron Microscopy Unit. Briefly, the embedded oocytes were post-fixed in 2% osmium tetroxide plus 0.8% potassium ferricyanide in 0.1M cacodylate buffer. After several rinses with 0.1M cacodylate buffer, the samples were dehydrated in methanol as described above. Samples were then infiltrated with Epon-Aradite (Ted Pella, Redding, CA): 30% Epon-Aradite in ethanol

for 2 hr, 50% for 4 hr, 75% overnight, and 100% for 1 day with 2X changes. Samples were polymerized at 60 °C for two days. Ultrathin sections (about 80 nm) were cut with a Reichert Ultracut E Microtome and collected on copper slot grids. Sections were counter-stained with uranyl acetate and lead citrate and examined under a FEI Tecnai12 transmission electron microscope operating with a beam energy of 120 keV. Images were acquired using a Gatan 2k × 2k cooled CCD camera.

Data availability. The sequencing data reported in this study has been deposited in the Gene Expression Omnibus website with accession code in process.

Results

Oocyte-specific knockout of *Exosc10* leads to female subfertility by disrupting oocyte maturation

Homozygous constitutive knockout of *Exosc10* in mice is embryonic lethal (Fig S1A, C). To study the function of EXOSC10 in oocyte development, we generated an *Exosc10* floxed allele by CRISPR/Cas9 and used *Zp3-cre* mice to specifically knock out *Exosc10* in growing oocytes. Two loxP sites surrounding exons 4-10 resulted in a deletion and a frame shift of the remaining coding sequence (Fig 1A). To increase loxP recombination efficiency, we used a mating strategy to present only one floxed allele for cre to obtain the desired oocyte-conditional knockout (*Flox/-; Zp3-cre*, cKO thereafter) (Fig 1B). qPCR of single oocytes confirmed the loss of *Exosc10* transcripts in cKO oocytes from the GV stage onward (Fig 1C; Fig S1B, D).

To assess female fertility affected by oocyte specific EXOSC10 depletion, we set harem breeders of cKO and control females with wildtype males for 6 months. Combining the records of 7 harems including 8 cKO females and 9 controls, the cKO females exhibited substantial subfertility with reduced pups (70 vs. 271) and litters (2.6 vs. 4.1) per female. The litter sizes also were significantly decreased in the cKO females (mean values of 3.3 vs. 7.3, Fig 1D). Intrigued by the subfertility, we investigated possible defects in oocyte growth, oocyte maturation and early embryogenesis. At 12 weeks, cKO and control females had indistinguishable ovaries in terms of weight, histology and antral follicle number (Fig S1E-H) which suggests normal oocyte growth. Although the diameter of the cKO oocytes was modestly decreased (Fig S1I), we concluded that the subfertility of cKO females is likely due to defects after the growth phase.

Next, we examined oocyte maturation and determined that GV oocytes collected from cKO females had deficient meiotic progression by 20 hr *ex vivo* culture (Fig S1J). Correspondingly, the number of ovulated eggs recovered following gonadotropin stimulation also was significantly decreased in cKO females (Fig S1K). We narrowed the defect to GVBD (Fig 1E-F). Although the mitotic organization center protein of the spindle appeared normal (Fig S1L), Lamin B persisted at GV+3hr in cKO oocytes, and the intensity of immunostaining was substantially increased at both GV and GV+3hr stages compared to controls (Fig 1G). We *in vitro* synthesized *Exosc10-mVenus* cRNA to rescue the cKO oocytes and found that EXOSC10-mVenus had nuclear localization in both oocytes and embryos (Fig S1M). Although the GVBD ratio did not revert to normal, the injected *Exosc10-mVenus* cRNA decreased lamin B intensity (Fig 1H-I). We conclude that GVBD is impaired in cKO oocytes.

We also evaluated pre-implantation development of the embryos derived from homozygous cKO females. In *ex vivo* culture of 1-cell embryos, there was decreased blastocyst formation at embryonic day 3.5 (E3.5). Many embryos had developmental delay from E1.5 to E3.5, and some of them arrested at the 2-cell stage (Fig S1N-O). In sum, oocyte specific EXOSC10

depletion causes substantial subfertility due to defective GVBD and embryos derived from cKO females progress abnormally during pre-implantation development.

EXOSC10 depletion dysregulates poly(A) RNA profile

To investigate the molecular basis of this phenotype, we sought to identify the types of RNA regulated by EXOSC10 in oocytes. EXOSC10 exhibits ribonuclease activity toward a range of poly(A) RNA molecules, including mRNA and rRNA (Lemieux et al., 2011; Tseng et al., 2018). We therefore used RNA FISH to quantify the poly(A) RNA with an oligo(dT) probe. In wildtype oocytes, there was a modest decrease during maturation from GV to GV+3hr maturation and then a sharp decrease during progression to the MII stage (Fig S2A-B) which is consistent with the known RNA degradation during oocyte maturation (Yu et al., 2016). Oocytes overexpressing *Exosc10-mVenus* had significantly decreased poly(A) compared to *mVenus* alone overexpression at both GV and GV+3hr stages, suggesting a role for EXOSC10 in degrading poly(A) RNA. However, when the ribonuclease catalytic sites were mutated (D313N and E315Q in EXOSC10), overexpression of the *dExosc10-mVenus* lost the ability to accelerate poly(A) RNA degradation (Fig S2C-D). On the other hand, the overall poly(A) RNA intensity in cKO oocytes showed no obvious change compared to controls, probably due to little transcription from the GV stage onward (Fig S2E-F). These results indicate that EXOSC10 participates in poly(A) RNA elimination during mouse oocyte maturation.

To characterize the dysregulated poly(A) RNA that account for the phenotype, we performed single oocyte RNA-seq at GV, GV+3hr and MII stages. The poly(A) RNA were isolated by oligo-dT beads (Fig 2A) and an equal amount of ERCC Spike-In Mix was added to each oocyte lysate to ensure library quality and to compare initial RNA quantities (Fig S3). In total, 71 oocytes (from 7 controls and 8 cKO mice) were sequenced, and 64 passed quality control. In normalizing oocyte total RNA with ERCC, we observed dependence on library size (Fig 2B) and used ERCC as the normalization reference for later differential analysis of gene expression. In addition to an overall mild delay in RNA degradation (Fig 2C), cKO oocytes exhibited distinct gene expression patterns as determined by pan-transcriptome expression heatmap (every 100th transcript after being ranked by expression level) and principal component analysis (Fig 2D-E). As expected, the nearly complete loss of *Exosc10* transcript in cKO oocytes was validated by RNA-seq (Fig 2F).

ERCC normalization allowed comparison of transcriptomes between stages of development. Within control oocytes, we identified 56 genes (ρ-adjust<0.01) that were downregulated from GV to GV+3hr. Using Gene Ontology (GO) analysis, these transcripts were associated with mitochondria, poly(A) RNA binding and protein transport through the endomembrane system. From GV+3hr to MII stage, we identified an additional 11,065 genes that were downregulated. There were almost no genes upregulated which is consistent with minimal transcription during oocyte maturation (Fig 2G-I). Differentially expressed genes in cKO and controls were further analyzed. At each stage, we identified more upregulated genes than downregulated genes (Fig 2J-L). Considering that EXOSC10 directly eliminates poly(A) RNA (Fig S2), the upregulated transcripts were more likely to be EXOSC10's substrates responsible for the phenotype. We performed GO analysis of the upregulated genes at GV and GV+3hr. The most prominent terms were associated with transcriptional control, RNA metabolism, endomembrane transport and meiosis (Fig 2M). All of these biologic processes occur during nuclear envelope breakdown (Guttinger et al., 2009) which links the dysregulated transcriptome in cKO oocytes with failure of GVBD.

Heterogeneity of the cKO oocytes underlies subfertility

We focused on RNA-seq results from GV and GV+3hr stages to investigate the effect of the *Exosc10* cKO on GVBD. The original PCA documented substantial variance within cKO oocytes

(Fig 2E) suggesting oocyte heterogeneity. It seemed plausible that greater dysregulation of the transcriptome would correlate with more reduced fertility of individual oocytes. Therefore, we performed PCA again using the 41 samples of control oocytes and cKO oocytes at both GV and GV+3hr stages and employed k-means clustering to define three groups (k=3). As expected, there was one group that included all the control oocytes in both GV and GV+3hr stages which is consistent with the high similarity between GV and GV+3hr of control oocytes analyzed in the original PCA (Fig 2E). The two other groups were designated cKO (major) and cKO (minor) according to their greater and lesser distances from the control group on the PCA plot (Fig 3A-B). By differential analysis of cKO (major) and cKO (minor) vs. control, we found that the cKO (major) group exhibited more upregulated genes than the cKO (minor) group (Fig 3C-D). The differentially expressed genes between cKO (major) and cKO (minor) groups were enriched for GO terms including transcription regulation, mitochondrion, cell cycle and endomembrane vesicles which recapitulated the observed differences in the original PCA plot (Fig 3E-F; Fig 2M). To confirm the stronger phenotype in cKO (major) compared to cKO (minor), we examined six genes that were markedly upregulated in the 6 GO terms enriched by cKO vs. control (Fig 2M). The abundance of transcripts from all six genes were significantly higher in the cKO (major) compared to the cKO (minor) group (Fig 3G). Thus, greater dysregulation of the transcriptome in individual oocytes decreased their potential fecundity.

cKO oocytes have disrupted endomembrane system

Nuclear envelope breakdown involves multiple components of the endomembrane system, including the ER, Golgi, endosomes and lysosomes (Audhya et al., 2007; Chung et al., 2018; Ivanov et al., 2013). Consistent with these finds, the GO analysis of the cKO RNA-seq highlighted intracellular vesicle trafficking. Therefore, we examined a range of cytoplasmic vesicles including endosomes, ER and lysosomes. Rab5-labeled early endosomes displayed abnormal aggregation and increased abundance in cKO oocytes (Fig 4A-B). In contrast, Rab7-labeled late endosomes were reduced (Fig 4C-D) suggesting insufficient endosome maturation (Poteryaev et al., 2010). Live imaging of oocytes treated by ER-Tracker had a reduced signal, whereas the Lyso-Tracker treated oocytes had increased signal. In sum, formation of the endomembrane system was disrupted due to EXOSC10 depletion (Fig 4E). This was confirmed by electron microscopy that documented vesicle aggregation close to the cytoplasmic membrane which contain endosome vesicles and mitochondria. These ultrastructural images confirmed the increased presence of Rab5-positive early endosomes (Fig 4F).

In the RNA-seq analyses, *Rab5a* transcripts were significantly increased in the cKO oocytes whereas *Rab7* transcripts were decreased (Fig 4G). The accumulative *Rab5a* upregulation and *Rab7* downregulation from cKO (minor) to cKO (major) could also be confirmed by visualizing their expression level on the PCA plot (Fig 4H). We tried to phenocopy the cKO oocytes by overexpressing *Rab5a-mVenus/Rab5c-mVenus* cRNA in GV oocytes. However, there was no obvious delay or arrest in *Rab5a-mVenus/Rab5c-mVenus* overexpressed oocytes compared with the *mVenus* overexpression controls (Fig S4A-B). Nor did we observed defects in endosome maturation (Fig S4C-D) indicating that the endosome failure was coupled to other impaired vesicle components. To conclude, the cKO oocytes exhibited extensive defects in the endomembrane system.

Inhibitory phosphorylated CDK1 persists in cKO oocytes to block lamina disassembly

The driving force of nuclear envelope breakdown is phosphorylation of nuclear lamina protein and nuclear pore components by active mitotic/meiotic kinases (Heald and McKeon, 1990; Peter et al., 1990). To obtain better insight into GVBD, we divided oocytes into three groups based on lamin B integrity: intact, GVBD (early) and GVBD (late). The intact phase had an even and continuous distribution of lamin B surrounding the nucleus and was widely present among

oocytes after 0 to 3 hr *ex vivo* incubation. The GVBD (early) group emerged ~1 hr, during which lamin B was still continuous (XY optical sections) but exhibiting much smaller enclosed areas and an unevenly shrunken pattern. Finally, after the nuclear envelop was breached by the spindle, lamin B became discontinuous and quickly disappeared, which defined the GVBD (late) phase. Lamin A/C staining precisely recapitulated that of lamin B (data not shown).

Given the well-studied control of CDK1 phosphorylation in meiosis, we hypothesized that the inhibitory phosphorylated CDK1 favors GV arrest while its elimination eventually results in GVBD. To demonstrate this, we explored the change of inhibitory phosphorylated CDK1 ($p^{T14/Y15}$CDK1) during wildtype GVBD. In oocytes at the intact phase, the $p^{T14/Y15}$CDK1 formed nuclear puncta. When entering GVBD (early) phase, the puncta pattern underwent a constant decrease and eventually disappeared during the GVBD (late) phase (Fig 5A-B). We then hypothesized that the $p^{T14/Y15}$CDK1 remained constant in cKO oocytes to block GVBD. At the GV stage, $p^{T14/Y15}$CDK1 in cKO oocytes was similar to the control group, At GV+3hr when most control oocytes finished GVBD and exhibited a low level of $p^{T14/Y15}$CDK1, the cKO oocytes retained $p^{T14/Y15}$CDK1 puncta of high intensity (Fig 5C-D). Thus, failure in transiting CDK1 phosphorylation from inhibitory to active results in the GV arrest in cKO oocytes.

Next, we analyzed phosphorylation of lamin A/C (p^{S22}lamin A/C) which is the direct substrate of active phosphorylated CDK1 (Heald and McKeon, 1990). After 1 hr *ex vivo* culture, p^{S22}lamin A/C displayed a nuclear puncta pattern in oocytes. Upon entering the GVBD (early) phase, p^{S22}lamin A/C increased its abundance with concomitant loss of punctate loci and co-localized with lamin A/C. After progressing to the GVBD (late) phase, lamin A/C and p^{S22}lamin A/C co-localized on the dissolving nuclear envelope albeit with decreased abundance (Fig 5E-F). These observations suggest that the activation of $p^{T14/Y15}$CDK1 increases p^{S22}lamin A/C, which results in nuclear envelope disassembly. In cKO oocytes, p^{S22}lamin A/C failed to change from puncta to perinuclear localization at GV+3hr and failed to accumulate, both of which appear necessary for entering the GVBD (late) phase (Fig 5G-H).

The inhibitory CDK1 phosphorylation may be regulated by upstream kinase activity, including PKA and WEE1/2 (Han and Conti, 2006; Oh et al., 2010). Our RNA-seq data documented that *Wee1* was upregulated significantly in cKO oocytes (log2FC 1.92 and 2.16 at GV and GV+3 hr, respectively, ρ-adjust < 0.01), potentially contributing the higher $p^{T14/Y15}$CDK1 level (Fig 5I). The significantly increased abundance of *Wee1* during the transition from cKO (minor) to cKO (major) was confirmed by visualizing its expression level on the PCA plot (Fig 5J). We also examined cAMP signaling which functions upstream of CDK1 phosphorylation to maintain the oocyte in a GV-intact state. However, cAMP levels and its known activators did not increase in cKO oocytes (Fig S5A-B). These observations are consistent with signaling pathways downstream of cAMP facilitating persistent inhibitory CDK1 phosphorylation. In conclusion, cKO oocytes had inappropriate CDK1 and lamin A/C phosphorylation regulation associated with the block to GVBD.

Discussion

RNA degradation plays a critical role in shaping the maternal transcriptome for functional transitions, perturbation of which can result in disrupted meiosis or failed pre-implantation development. In our study, we generated oocyte-specific, conditional *Exosc10* knockout mice in which the maternal transcriptome was dysregulated. We document an important role for EXOSC10 in orchestrating endomembrane components and meiotic cell cycle control through poly(A) RNA degradation. The absence of EXOSC10 directly leads to a decline in female fecundity.

Fully grown GV and GVBD oocytes are transcriptionally quiescent and genetic defects in normal degradation of RNA result in transcriptome dysregulation (Dumdie et al., 2018; Yu et al., 2016). In gene-edited mouse models that affect RNA metabolism, overall RNA profile is changed as a result of direct and secondary responses to the mutant genes. For example, oocyte-specific knockout of *Zfp36l2*, an activator of mRNA decay, disturbs a set of histone modifiers necessary to inhibit chromatin silencing at the end of oocyte growth (Dumdie et al., 2018). Knockout of *Btg4*, a scaffold protein bridging translation and deadenylation components, disrupts the translation of many RNAs and prevents morphologically normal egg from being fertilized (Yu et al., 2016). To obtain information on RNAs that undergo regulated degradation during oocyte maturation, we selected a gene with known RNase activity, EXOSC10, and confirmed poly(A) RNA as EXOSC10 substrates through both RNA FISH and RNA-seq. Combining phenotypic characterization and sequence analysis, we conclude that the EXOSC10-depleted GV oocytes have less potential to organize germinal vesicle breakdown because of defects in endomembrane trafficking and CDK1 phosphorylation activation which disrupts meiosis I resumption.

In our study, we introduced ERCC spike-in normalization for single oocyte RNA-seq analysis. This method not only provides a stringent criterion for library quality evaluation, but also allows comparison among libraries that vary considerably in size. In control oocytes, we observed a decrease in the abundance of 56 transcripts as oocytes progressed from the GV to the GV+3hr stage. Among them, 12 transcripts encoded ribosomal proteins, potentially preparing the poly(A) RNA for degradation and/or translation to provide proteins necessary for the growth-to-maturation transition. The other transcripts encoded proteins that were related to mitochondria and protein transport which are involved extensively in oocyte quality control and aging (Igarashi et al., 2015). We also observed a dramatic elimination of RNAs during oocyte progression from GV+3hr to the MII stage, consistent with known biological shrinkage of total RNA in maturing oocytes. Similar to the mutants of the other RNA regulators, we observed an overall change in RNA abundance in *Exosc10* cKO oocytes, including a dramatic upregulation of many genes, and a relatively milder downdegulation which may reflect secondary effects. The immediate dysregulation of the GV oocyte transcriptome after EXOSC10 depletion indicates its importance in oogenesis.

Mechanistically, our study shows that EXOSC10 sculpts the transcriptome to affect endomembrane components necessary for nuclear envelope breakdown. The endomembrane components participate in the maturation of oocytes including: endosomes that balance GPR-cAMP signaling for meiosis arrest control (Lowther et al., 2011); Golgi that fragment for assisting spindle initiation (Moreno et al., 2002); ER that reorganizes from cytoplasmic network into cortical clusters for meiosis division (FitzHarris et al., 2007); and lysosomes along with autophagosomes that actively degrade proteins, lipids and sugars (Shin et al., 2017). In control oocytes, we identified the initial reframing of the endomembrane system in growth-to-maturation transition (GV to GV+3hr), including the downregulation of *Sec61g* and *Sec61b*. It has been reported that overexpression of *Sec61* does not affect post-mitotic nuclear envelope reorganization (Anderson and Hetzer, 2008). However, given its tight association with NE-ER exchange, our result indicates that *Sec61* decrease may be required for NE disassembly. In EXOSC10 depleted oocytes, endomembrane components exhibit substantial defects. We identified several Rab family members upregulated in cKO oocytes, including Rab5a, Rab5b, Rab34 and Rab37, which are known as molecular switches in regulating intracellular membrane trafficking. The enlarged early endosome (Rab5) suggests the defects of endosome maturation. *Rab34* upregulation is known to promote phagosome fusion with lysosome; concomitantly, upregulated *Rab37* and *Atg16l2* can also directly activate the phagosome formation (Ishibashi et al., 2011; Sheng et al., 2018), collectively suggesting that the enlarged lysosome in cKO oocytes may originate from activated phagocytosis (Kasmapour et al., 2012). An important

future study should address coupling between different vesicles which will add to the understanding of the role of the endomembrane system in oocyte quality control.

From the subfertility phenotype of the *Exosc10* cKO mutant, we suspected heterogeneity among the cKO oocytes which is confirmed by the single oocyte RNA-seq results. The cKO (minor) to cKO (major) difference successfully demonstrates an exacerbation of the phenotype, including a growing number of differentially expressed genes that affect important pathways for maturation. The mechanism underlying this heterogeneity remains unclear. One possibility is that other RNA exosome-associated RNases, such as DIS3, could compensate for the loss of EXOSC10. In control groups, *Dis3* transcript increases from GV to GV+3hr, potentiating its functions for oocyte maturation. However, *Exosc10* cKO oocytes lack an increase in *Dis3* abundance which makes it unlikely that DIS3 compensates for the loss of EXOSC10. Thus, there may be another RNase functioning redundantly for EXOSC10. Another possibility could come from stochastic variations of oocyte development. For example, variance in chromosome condensation at the end of oocyte growth may differentially affect gene silencing and affect nuclear envelope breakdown. Once key transcripts are below a functional threshold, oocytes may be able to proceed to meiosis with minimal amounts of EXOSC10.

In conclusion, our data document transcriptome remodeling in the transition from oocyte growth to maturation. We demonstrate that EXOSC10-mediated degradation of active poly(A) RNA underlies the transition by coordinating the transcriptome for endomembrane trafficking and resumption of meiosis. These results are consistent with a growing body of experimental data that RNA degradation governs the later stages of oogenesis while putting the oocyte gain of developmental potential into a more refined time window.

Acknowledgements

We appreciate the critical reading of the manuscript by Shaohe Wang, Ph.D. and Yangu Zhao, Ph.D. as well as useful discussions with all the members of the Jurrien Dean lab.
This research was supported by the Intramural Research Program of NIH, National Institutes of Diabetes and Digestive and Kidney Diseases (1ZIADK015603).

Author contributions

D.W. and J.D conceived the project. D.W. performed the experiments and C.P. provided bioinformatic expertise. D.W. and J.D. wrote manuscript with input from C.P.

Competing Interests

The authors declare no competing interests.

Figure legends

Figure 1. Oocyte-specific knockout of *Exosc10* causes female subfertility by impairing germinal vesicle breakdown during oocyte maturation. (**A**) Schematic of strategy to generate an *Exosc10* floxed allele using CRISPR/Cas9. Two loxP sites were inserted to bracket exons 4-10. (**B**) Mating strategy to obtain oocyte-specific conditional knockouts of *Exosc10* (cKO). Siblings with other genotypes were used as controls. (**C**) RT-qPCR of *Exosc10* in single oocytes obtained from controls and cKO mice. (**D**) Dot plot of individual litter sizes over 6 months of harem breeding of controls and cKO females with wildtype males. The number in parenthesis is the number of females having the indicated genotypes. The number of pups born is indicated below each group. (**E**) Bright-field images cKO and controls oocytes cultured *ex vivo* for 0 (GV) or 3 hr (GV+3hr). (**F**) Percentage of GVBD oocytes in **E**. Number of oocytes indicated below each group. (**G**) Confocal fluorescence and brightfield/DAPI images of oocyte after lamin B immunostaining at GV (top) and GV+3hr (bottom) stages. Lamin B and DAPI are maximum intensity projections and bright-field images are single optical sections containing the nucleus. Quantification of lamin B fluorescence is on the right. The numbers of oocytes from at least 3 females are indicated below each group. The horizontal lines inside the violins represent the median and quartiles. (**H**) Confocal fluorescence images of lamin B immunostaining at GV+3hr stage. Control oocytes were un-injected; cKO oocytes were microinjected with either *mVenus* (*mV*) or *Exosc10-mVenus* (*Exo10-mV*) cRNA. (**I**) Quantification of lamin B fluorescence in **H**. The numbers of oocytes from at least 3 females are indicated below each group. The horizontal lines represent the mean and standard deviation in **D**, **I**. **** ρ<0.0001 in **D**, two-tailed Student's t-test. **** ρ<0.0001, *** ρ<0.001, * ρ<0.05, n.s. no significance in **G**, **I**, ordinary one-way ANOVA. Scale bars: 100 μm in **E**; 20 μm in **G**, **H**.

Figure 2. *Exosc10^{cKO}* oocytes exhibit dysregulated transcriptome during oocyte maturation. (A) Schematic illustrating the pipeline of single oocyte RNA-seq. After individual oocyte lysis, oligo-dT beads captured poly(A) RNAs for library construction and sequencing. Genomic DNA determines genotype. (**B**) Total RNA levels are normalized for each library by ERCC RNA spike-in mix. (**C**) Further normalization of total RNA level in **B** by the mean value of GV stage within each genotype. (**D**) Heatmap of all libraries (genes are ranked from highest to lowest expression level and every 100th transcript was selected to represent the entire transcriptome, color-coded according to the transcription level). (**E**) Principal component analysis (PCA) of the 64 libraries. Each dot represents one library, color coded by genotype and stage. (**F**) Log_2 fold change of *Exosc10* and *Gapdh* with cKO vs. control. The bars and lines are log_2 fold change and standard error of the mean from DESeq2 analyses. **** ρ<0.0001, n.s. no significance, which are the ρ-adjust values in DESeq2 analysis. (**G-H**) MA-plots of transcript changes from GV to GV+3hr, and from GV+3hr to MII stage in control groups. The upregulated and downregulated gene numbers in each comparison are labeled by red and blue, respectively (both have ρ-adjust <0.01). (**I**) Gene ontology of upregulated genes in **G**. (**J-L**) MA-plots of transcript changes in cKO vs. control oocytes at GV, GV+3hr and MII stages. The upregulated and downregulated gene numbers in each comparison are labeled by red and blue, respectively (ρ-adjust <0.01). (**M**) Gene ontology of the upregulated genes with log_2 fold-change more than 1 in **J-K**.

Figure 3. Transcriptome heterogeneity of *Exosc10^{cKO}* oocytes underlies the subfertility. (A) Principal component analysis (PCA) of 41 libraries of control oocytes and cKO oocytes at both GV and GV+3hr stages. Subsequently the 41 libraries were sub-clustered by k-means

algorithm into 3 groups, including control, cKO (major) and cKO (minor). Perimeter line color-coded to indicate library source. Through this clustering analysis, the GV and GV+3hr stages were combined by the same genotype. (**B**) Sample distance matrix of the 41 libraries in **A**. (**C**-**D**) MA-plots of cKO (major) vs. control and cKO (minor) vs. control libraries. (**E**) MA-plot of cKO (major) vs. cKO (minor). The upregulated and downregulated gene numbers in each comparison are labeled by red and blue, respectively (ρ-adjust <0.01). (**F**) Gene ontology of up regulated genes with $\log_2$ fold change more than 1 in **E**. (**G**) PCA plots of **A** that is color-coded by the expression level of each transcript in individual oocytes. Perimeter line is color-coded to indicate library source.

Figure 4. *Exosc10*^{cKO} oocytes have disrupted endomembrane system. (**A**) Immunostaining of oocyte Rab5A/C (early endosome) at the GV stage. (**B**) Quantification of Rab5A/C vesicle fluorescence intensity in **A**. (**C**) Same as **A**, but for Rab7 (late endosome). (**D**) Quantification of Rab7 vesicle intensities in **C**. For the violin plots in **B**, **D**, the horizontal lines inside the violins represent the median and the dash lines represent the quartiles. **** ρ<0.0001, two-tailed Student's t-test. Number of oocytes is indicated below each group. (**E**) Live imaging of oocytes derived from control and cKO incubated with ER-Tracker and Lyso-Tracker. The untreated group is in the right column. (**F**) Electron microscopy showing vesicle aggregation close to the plasma membrane. Red dashed line indicates the clustered vesicles. (**G**) A bar graph showing mean and standard error of $\log_2$ fold change of *Rab5A*, *Rab5C* and *Rab7* transcripts from single oocyte RNA-seq. **** ρ<0.0001, n.s. no significance, which are the ρ-adjust values by DESeq2 analysis. **(H)** PCA plots of *Rab 5* (left) and *Rab7* (right) that is color-coded by the expression level of each transcript in individual oocytes. Perimeter line is color-coded to indicate library source. Scale bars: 20 μm in **A**, **C**; 100 μm in **F**; 1 μm in **E**. Arbitrary fluorescence units (au) in **B**, **D**.

Figure 5. *Exosc10*^{cKO} oocytes with inhibitory CDK1 lack lamina phosphorylation and GVBD. (**A**) Confocal fluorescence images of inhibitory phosphorylated CDK1 ($p^{T14/Y15}$CDK1), bright-field and DAPI in wildtype oocytes at different time points during *ex vivo* culture and GVBD. Oocytes were collected every 30 min and combined into three stages: 0-1 hr includes 0 and 0.5 hr stages; 1-2 hr includes 1 and 1.5 hr stages; 2-3 hr includes 2, 2.5 and 3 hr stages. (**B**) Quantification of $p^{T14/Y15}$CDK1 in **A**. Number of oocytes are indicated above each group. At each time points, oocytes are clustered as Intact, GVBD (early) or GVBD (late) based on lamin B integrity. (**C**) Representative images of $p^{T14/Y15}$CDK1 in oocytes at GV and GV+3hr stages derived from control and cKO mice. (**D**) Quantification of $p^{T14/Y15}$CDK1 fluorescence intensities in **C**. The numbers of oocytes from at least three experiments are indicated above each group. (**E**) Same as **A**, but for p^{S22}lamin A/C (p^{S22}L-A/C). (**F**) Same as **B**, but for p^{S22}lamin A/C. (**G**) Same as **C**, but for p^{S22}lamin A/C only at GV+3hr. (**H**) Same as **D**, but for p^{S22}lamin A/C only at GV+3hr. (**I**) Bar graph of mean and standard error of $\log_2$ fold change of *Cdk1*, *Prkaca*, *Wee1* transcripts from the single oocyte RNA-seq. **** ρ<0.0001, n.s. no significance, which are the ρ-adjust values by DESeq2 analysis. The horizontal lines in **B**, **D**, **F**, **H** represent the median and quartiles. Scale bars: 20 μm in **A**, **C**, **E**, **G**. **(J)** PCA plots of *Wee1* that is color-coded by the expression level in each oocyte. Perimeter line is color-coded to indicate library source. (**K**) Working model of the characterized defects in *Exosc10*^{cKO} oocytes in which the absence of the EXOSC10 delays degradation of maternal transcripts which prevents activation of CDK1. In the absence of this active cell cycle component, degradation of nuclear lamin B is delayed which preserves the nuclear envelope and impairs GVBD leading to decreased female fecundity.

Reference

Anderson, D.J., and Hetzer, M.W. (2008). Reshaping of the endoplasmic reticulum limits the rate for nuclear envelope formation. The Journal of cell biology 182, 911-924.
Dumdie, J.N., Cho, K., Ramaiah, M., Skarbrevik, D., Mora-Castilla, S., Stumpo, D.J., Lykke-Andersen, J., Laurent, L.C., Blackshear, P.J., Wilkinson, M.F., et al. (2018). Chromatin Modification and Global Transcriptional Silencing in the Oocyte Mediated by the mRNA Decay Activator ZFP36L2. Developmental cell 44, 392-402 e397.
FitzHarris, G., Marangos, P., and Carroll, J. (2007). Changes in endoplasmic reticulum structure during mouse oocyte maturation are controlled by the cytoskeleton and cytoplasmic dynein. Developmental biology 305, 133-144.
Igarashi, H., Takahashi, T., and Nagase, S. (2015). Oocyte aging underlies female reproductive aging: biological mechanisms and therapeutic strategies. Reprod Med Biol 14, 159-169.
Ishibashi, K., Fujita, N., Kanno, E., Omori, H., Yoshimori, T., Itoh, T., and Fukuda, M. (2011). Atg16L2, a novel isoform of mammalian Atg16L that is not essential for canonical autophagy despite forming an Atg12-5-16L2 complex. Autophagy 7, 1500-1513.
Kasmapour, B., Gronow, A., Bleck, C.K., Hong, W., and Gutierrez, M.G. (2012). Size-dependent mechanism of cargo sorting during lysosome-phagosome fusion is controlled by Rab34. Proceedings of the National Academy of Sciences of the United States of America 109, 20485-20490.
Lewandoski, M., Wassarman, K.M., and Martin, G.R. (1997). Zp3-cre, a transgenic mouse line for the activation or inactivation of loxP-flanked target genes specifically in the female germ line. Current biology : CB 7, 148-151.
Lowther, K.M., Nikolaev, V.O., and Mehlmann, L.M. (2011). Endocytosis in the mouse oocyte and its contribution to cAMP signaling during meiotic arrest. Reproduction 141, 737-747.
Moreno, R.D., Schatten, G., and Ramalho-Santos, J. (2002). Golgi apparatus dynamics during mouse oocyte in vitro maturation: effect of the membrane trafficking inhibitor brefeldin A. Biology of reproduction 66, 1259-1266.
Sheng, Y., Song, Y., Li, Z., Wang, Y., Lin, H., Cheng, H., and Zhou, R. (2018). RAB37 interacts directly with ATG5 and promotes autophagosome formation via regulating ATG5-12-16 complex assembly. Cell Death Differ 25, 918-934.
Shin, S.W., Vogt, E.J., Jimenez-Movilla, M., Baibakov, B., and Dean, J. (2017). Cytoplasmic cleavage of DPPA3 is required for intracellular trafficking and cleavage-stage development in mice. Nature communications 8, 1643.
Veselovska, L., Smallwood, S.A., Saadeh, H., Stewart, K.R., Krueger, F., Maupetit-Mehouas, S., Arnaud, P., Tomizawa, S., Andrews, S., and Kelsey, G. (2015). Deep sequencing and de novo assembly of the mouse oocyte transcriptome define the contribution of transcription to the DNA methylation landscape. Genome biology 16, 209.
Yu, C., Ji, S.Y., Sha, Q.Q., Dang, Y., Zhou, J.J., Zhang, Y.L., Liu, Y., Wang, Z.W., Hu, B., Sun, Q.Y., et al. (2016). BTG4 is a meiotic cell cycle-coupled maternal-zygotic-transition licensing factor in oocytes. Nature structural & molecular biology 23, 387-394.
Macaulay, I.C., Teng, M.J., Haerty, W., Kumar, P., Ponting, C.P., and Voet, T. (2016). Separation and parallel sequencing of the genomes and transcriptomes of single cells using G&T-seq. Nature protocols 11, 2081-2103.
Audhya, A., Desai, A., and Oegema, K. (2007). A role for Rab5 in structuring the endoplasmic reticulum. The Journal of cell biology 178, 43-56.
Chung, G.H.C., Domart, M.C., Peddie, C., Mantell, J., McLaverty, K., Arabiotorre, A., Hodgson, L., Byrne, R.D., Verkade, P., Arkill, K., et al. (2018). Acute depletion of diacylglycerol from the cis-Golgi affects localized nuclear envelope morphology during mitosis. Journal of lipid research 59, 1402-1413.

Guttinger, S., Laurell, E., and Kutay, U. (2009). Orchestrating nuclear envelope disassembly and reassembly during mitosis. Nature reviews Molecular cell biology 10, 178-191.
Han, S.J., and Conti, M. (2006). New pathways from PKA to the Cdc2/cyclin B complex in oocytes: Wee1B as a potential PKA substrate. Cell cycle 5, 227-231.
Heald, R., and McKeon, F. (1990). Mutations of phosphorylation sites in lamin A that prevent nuclear lamina disassembly in mitosis. Cell 61, 579-589.
Ivanov, A., Pawlikowski, J., Manoharan, I., van Tuyn, J., Nelson, D.M., Rai, T.S., Shah, P.P., Hewitt, G., Korolchuk, V.I., Passos, J.F., et al. (2013). Lysosome-mediated processing of chromatin in senescence. The Journal of cell biology 202, 129-143.
Lemieux, C., Marguerat, S., Lafontaine, J., Barbezier, N., Bahler, J., and Bachand, F. (2011). A Pre-mRNA degradation pathway that selectively targets intron-containing genes requires the nuclear poly(A)-binding protein. Molecular cell 44, 108-119.
Oh, J.S., Han, S.J., and Conti, M. (2010). Wee1B, Myt1, and Cdc25 function in distinct compartments of the mouse oocyte to control meiotic resumption. The Journal of cell biology 188, 199-207.
Peter, M., Nakagawa, J., Doree, M., Labbe, J.C., and Nigg, E.A. (1990). In vitro disassembly of the nuclear lamina and M phase-specific phosphorylation of lamins by cdc2 kinase. Cell 61, 591-602.
Poteryaev, D., Datta, S., Ackema, K., Zerial, M., and Spang, A. (2010). Identification of the switch in early-to-late endosome transition. Cell 141, 497-508.
Tseng, C.K., Wang, H.F., Schroeder, M.R., and Baumann, P. (2018). The H/ACA complex disrupts triplex in hTR precursor to permit processing by RRP6 and PARN. Nature communications 9, 5430.
Yu, C., Ji, S.Y., Sha, Q.Q., Dang, Y., Zhou, J.J., Zhang, Y.L., Liu, Y., Wang, Z.W., Hu, B., Sun, Q.Y., et al. (2016). BTG4 is a meiotic cell cycle-coupled maternal-zygotic-transition licensing factor in oocytes. Nature structural & molecular biology 23, 387-394.
Anderson, D.J., and Hetzer, M.W. (2008). Reshaping of the endoplasmic reticulum limits the rate for nuclear envelope formation. The Journal of cell biology *182*, 911-924.
Audhya, A., Desai, A., and Oegema, K. (2007). A role for Rab5 in structuring the endoplasmic reticulum. The Journal of cell biology *178*, 43-56.
Burns, K.H., Viveiros, M.M., Ren, Y., Wang, P., DeMayo, F.J., Frail, D.E., Eppig, J.J., and Matzuk, M.M. (2003). Roles of NPM2 in chromatin and nucleolar organization in oocytes and embryos. Science *300*, 633-636.
Carneiro, T., Carvalho, C., Braga, J., Rino, J., Milligan, L., Tollervey, D., and Carmo-Fonseca, M. (2007). Depletion of the yeast nuclear exosome subunit Rrp6 results in accumulation of polyadenylated RNAs in a discrete domain within the nucleolus. Molecular and cellular biology *27*, 4157-4165.
Chung, G.H.C., Domart, M.C., Peddie, C., Mantell, J., McLaverty, K., Arabiotorre, A., Hodgson, L., Byrne, R.D., Verkade, P., Arkill, K.*, et al.* (2018). Acute depletion of diacylglycerol from the cis-Golgi affects localized nuclear envelope morphology during mitosis. Journal of lipid research *59*, 1402-1413.
Domingo-Prim, J., Endara-Coll, M., Bonath, F., Jimeno, S., Prados-Carvajal, R., Friedlander, M.R., Huertas, P., and Visa, N. (2019). EXOSC10 is required for RPA assembly and controlled DNA end resection at DNA double-strand breaks. Nature communications *10*, 2135.
Dumdie, J.N., Cho, K., Ramaiah, M., Skarbrevik, D., Mora-Castilla, S., Stumpo, D.J., Lykke-Andersen, J., Laurent, L.C., Blackshear, P.J., Wilkinson, M.F.*, et al.* (2018). Chromatin Modification and Global Transcriptional Silencing in the Oocyte Mediated by the mRNA Decay Activator ZFP36L2. Developmental cell *44*, 392-402 e397.
FitzHarris, G., Marangos, P., and Carroll, J. (2007). Changes in endoplasmic reticulum structure during mouse oocyte maturation are controlled by the cytoskeleton and cytoplasmic dynein. Developmental biology *305*, 133-144.
Guttinger, S., Laurell, E., and Kutay, U. (2009). Orchestrating nuclear envelope disassembly and reassembly during mitosis. Nature reviews Molecular cell biology *10*, 178-191.

Han, S.J., and Conti, M. (2006). New pathways from PKA to the Cdc2/cyclin B complex in oocytes: Wee1B as a potential PKA substrate. Cell cycle *5*, 227-231.
Hartley, J.L., Zachos, N.C., Dawood, B., Donowitz, M., Forman, J., Pollitt, R.J., Morgan, N.V., Tee, L., Gissen, P., Kahr, W.H.A*., et al.* (2010). Mutations in TTC37 Cause Trichohepatoenteric Syndrome (Phenotypic Diarrhea of Infancy). Gastroenterology *138*, 2388-2398.
Heald, R., and McKeon, F. (1990). Mutations of phosphorylation sites in lamin A that prevent nuclear lamina disassembly in mitosis. Cell *61*, 579-589.
Igarashi, H., Takahashi, T., and Nagase, S. (2015). Oocyte aging underlies female reproductive aging: biological mechanisms and therapeutic strategies. Reprod Med Biol *14*, 159-169.
Ishibashi, K., Fujita, N., Kanno, E., Omori, H., Yoshimori, T., Itoh, T., and Fukuda, M. (2011). Atg16L2, a novel isoform of mammalian Atg16L that is not essential for canonical autophagy despite forming an Atg12-5-16L2 complex. Autophagy *7*, 1500-1513.
Ivanov, A., Pawlikowski, J., Manoharan, I., van Tuyn, J., Nelson, D.M., Rai, T.S., Shah, P.P., Hewitt, G., Korolchuk, V.I., Passos, J.F*., et al.* (2013). Lysosome-mediated processing of chromatin in senescence. The Journal of cell biology *202*, 129-143.
Jamin, S.P., Petit, F.G., Kervarrec, C., Smagulova, F., Illner, D., Scherthan, H., and Primig, M. (2017). EXOSC10/Rrp6 is post-translationally regulated in male germ cells and controls the onset of spermatogenesis. Scientific reports *7*, 15065.
Jose-Miller, A.B., Boyden, J.W., and Frey, K.A. (2007). Infertility. American family physician *75*, 849-856.
Kageyama, S., Liu, H., Kaneko, N., Ooga, M., Nagata, M., and Aoki, F. (2007). Alterations in epigenetic modifications during oocyte growth in mice. Reproduction *133*, 85-94.
Kasmapour, B., Gronow, A., Bleck, C.K., Hong, W., and Gutierrez, M.G. (2012). Size-dependent mechanism of cargo sorting during lysosome-phagosome fusion is controlled by Rab34. Proceedings of the National Academy of Sciences of the United States of America *109*, 20485-20490.
Kishimoto, T. (2018). MPF-based meiotic cell cycle control: Half a century of lessons from starfish oocytes. Proc Jpn Acad Ser B Phys Biol Sci *94*, 180-203.
Knight, J.R.P., Bastide, A., Peretti, D., Roobol, A., Roobol, J., Mallucci, G.R., Smales, C.M., and Willis, A.E. (2016). Cooling-induced SUMOylation of EXOSC10 down-regulates ribosome biogenesis. Rna *22*, 623-635.
Lemieux, C., Marguerat, S., Lafontaine, J., Barbezier, N., Bahler, J., and Bachand, F. (2011). A Pre-mRNA degradation pathway that selectively targets intron-containing genes requires the nuclear poly(A)-binding protein. Molecular cell *44*, 108-119.
Liu, J., Prunuske, A.J., Fager, A.M., and Ullman, K.S. (2003). The COPI complex functions in nuclear envelope breakdown and is recruited by the nucleoporin Nup153. Developmental cell *5*, 487-498.
Lowther, K.M., Nikolaev, V.O., and Mehlmann, L.M. (2011). Endocytosis in the mouse oocyte and its contribution to cAMP signaling during meiotic arrest. Reproduction *141*, 737-747.
Macaulay, I.C., Teng, M.J., Haerty, W., Kumar, P., Ponting, C.P., and Voet, T. (2016). Separation and parallel sequencing of the genomes and transcriptomes of single cells using G&T-seq. Nature protocols *11*, 2081-2103.
Macklon, N.S., Geraedts, J.P., and Fauser, B.C. (2002). Conception to ongoing pregnancy: the 'black box' of early pregnancy loss. Human reproduction update *8*, 333-343.
Metchat, A., Akerfelt, M., Bierkamp, C., Delsinne, V., Sistonen, L., Alexandre, H., and Christians, E.S. (2009). Mammalian heat shock factor 1 is essential for oocyte meiosis and directly regulates Hsp90alpha expression. The Journal of biological chemistry *284*, 9521-9528.
Moreno, R.D., Schatten, G., and Ramalho-Santos, J. (2002). Golgi apparatus dynamics during mouse oocyte in vitro maturation: effect of the membrane trafficking inhibitor brefeldin A. Biology of reproduction *66*, 1259-1266.

Oh, J.S., Han, S.J., and Conti, M. (2010). Wee1B, Myt1, and Cdc25 function in distinct compartments of the mouse oocyte to control meiotic resumption. The Journal of cell biology *188*, 199-207.
Pefanis, E., Wang, J., Rothschild, G., Lim, J., Kazadi, D., Sun, J., Federation, A., Chao, J., Elliott, O., Liu, Z.P.*, et al.* (2015). RNA exosome-regulated long non-coding RNA transcription controls super-enhancer activity. Cell *161*, 774-789.
Peter, M., Nakagawa, J., Doree, M., Labbe, J.C., and Nigg, E.A. (1990). In vitro disassembly of the nuclear lamina and M phase-specific phosphorylation of lamins by cdc2 kinase. Cell *61*, 591-602.
Poteryaev, D., Datta, S., Ackema, K., Zerial, M., and Spang, A. (2010). Identification of the switch in early-to-late endosome transition. Cell *141*, 497-508.
Rolfsmeier, M.L., Laughery, M.F., and Haseltine, C.A. (2011). Repair of DNA double-strand breaks induced by ionizing radiation damage correlates with upregulation of homologous recombination genes in Sulfolobus solfataricus. Journal of molecular biology *414*, 485-498.
Rudnik-Schöneborn, S., Senderek, J., Jen, J.C., Houge, G., Seeman, P., Puchmajerová, A., Graul-Neumann, L., Seidel, U., Korinthenberg, R., Kirschner, J.*, et al.* (2013). Pontocerebellar hypoplasia type 1: Clinical spectrum and relevance of EXOSC3 mutations. Neurology *80*, 438-446.
Sheng, Y., Song, Y., Li, Z., Wang, Y., Lin, H., Cheng, H., and Zhou, R. (2018). RAB37 interacts directly with ATG5 and promotes autophagosome formation via regulating ATG5-12-16 complex assembly. Cell Death Differ *25*, 918-934.
Shin, S.W., Vogt, E.J., Jimenez-Movilla, M., Baibakov, B., and Dean, J. (2017). Cytoplasmic cleavage of DPPA3 is required for intracellular trafficking and cleavage-stage development in mice. Nature communications *8*, 1643.
Tseng, C.K., Wang, H.F., Schroeder, M.R., and Baumann, P. (2018). The H/ACA complex disrupts triplex in hTR precursor to permit processing by RRP6 and PARN. Nature communications *9*, 5430.
van Dijk, E.L., Schilders, G., and Pruijn, G.J. (2007). Human cell growth requires a functional cytoplasmic exosome, which is involved in various mRNA decay pathways. Rna *13*, 1027-1035.
Wasielak, M., Wiesak, T., Bogacka, I., Jalali, B.M., and Bogacki, M. (2016). Zygote arrest 1, nucleoplasmin 2, and developmentally associated protein 3 mRNA profiles throughout porcine embryo development in vitro. Theriogenology *86*, 2254-2262.
Weissbach, S., Langer, C., Puppe, B., Nedeva, T., Bach, E., Kull, M., Bargou, R., Einsele, H., Rosenwald, A., Knop, S.*, et al.* (2015). The molecular spectrum and clinical impact of DIS3 mutations in multiple myeloma. Br J Haematol *169*, 57-70.
Yu, C., Ji, S.Y., Sha, Q.Q., Dang, Y., Zhou, J.J., Zhang, Y.L., Liu, Y., Wang, Z.W., Hu, B., Sun, Q.Y.*, et al.* (2016). BTG4 is a meiotic cell cycle-coupled maternal-zygotic-transition licensing factor in oocytes. Nature structural & molecular biology *23*, 387-394.

Figure 1

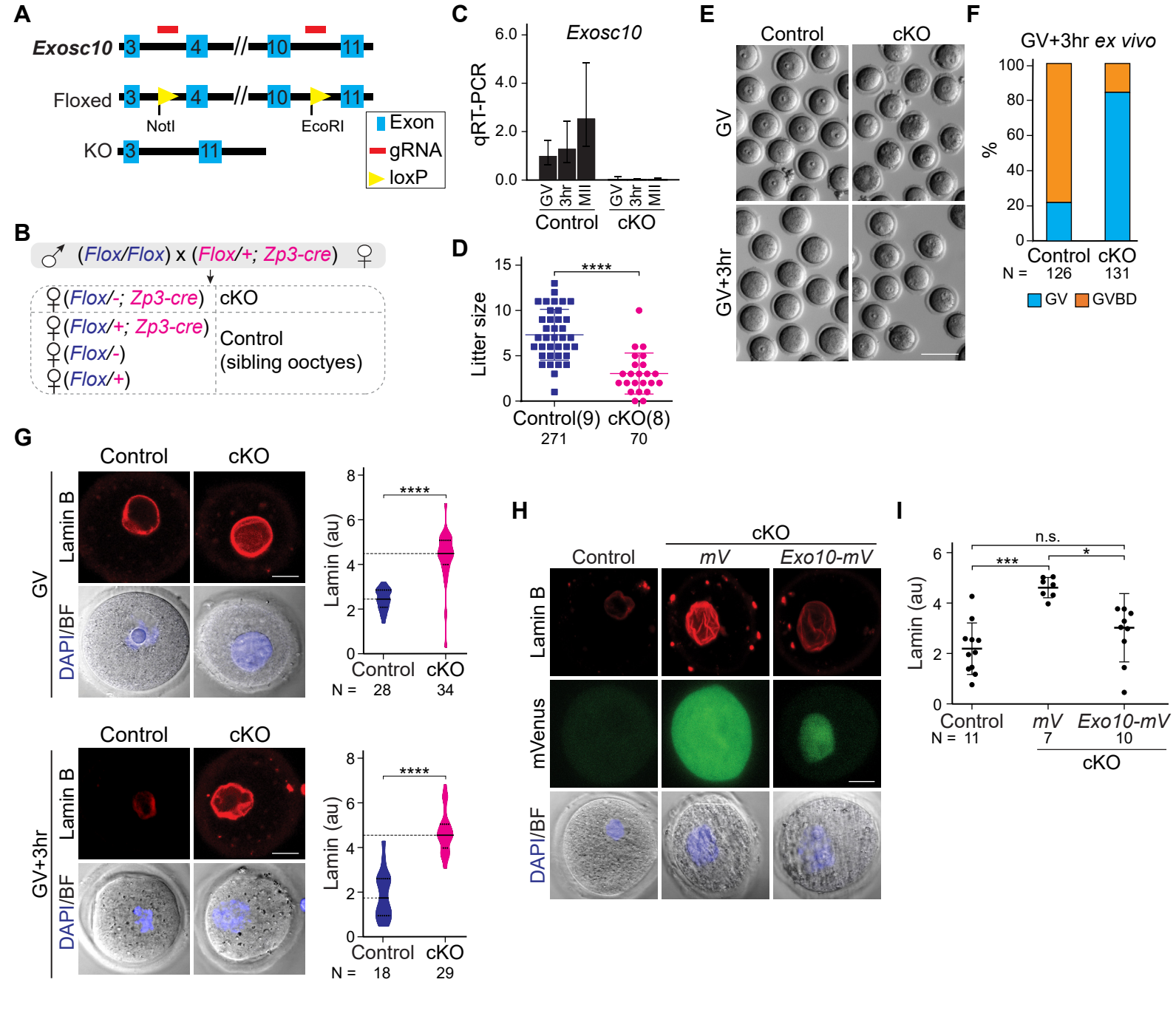
A
Exosc10
3
4
10
11
Floxed
NotI
EcoRI
KO
Exon
gRNA
loxP
B
♂ (Flox/Flox) x (Flox/+; Zp3-cre) ♀
♀(Flox/-; Zp3-cre)
cKO
♀♀(Flox/+; Zp3-cre)
♀♀(Flox/-)
♀♀(Flox/+)
Control
(sibling ooctyes)
C
Exosc10
qRT-PCR
6.0
4.0
2.0
0.0
GV
3hr
MII
Control
cKO
D
Litter size
15
10
5
0
****
Control(9)
271
cKO(8)
70
E
Control
cKO
GV
GV+3hr
F
GV+3hr ex vivo
%
100
80
60
40
20
0
Control
cKO
N = 126
131
GV
GVBD
G
Control
cKO
GV
Lamin B
DAPI/BF
Lamin (au)
8
6
4
2
0
****
Control
cKO
N = 28
34
GV+3hr
Lamin B
DAPI/BF
Lamin (au)
****
Control
cKO
N = 18
29
H
cKO
Control
mV
Exo10-mV
Lamin B
mVenus
DAPI/BF
I
Lamin (au)
n.s.
***
*
Control
mV
Exo10-mV
N = 11
7
10
cKO

Figure 2

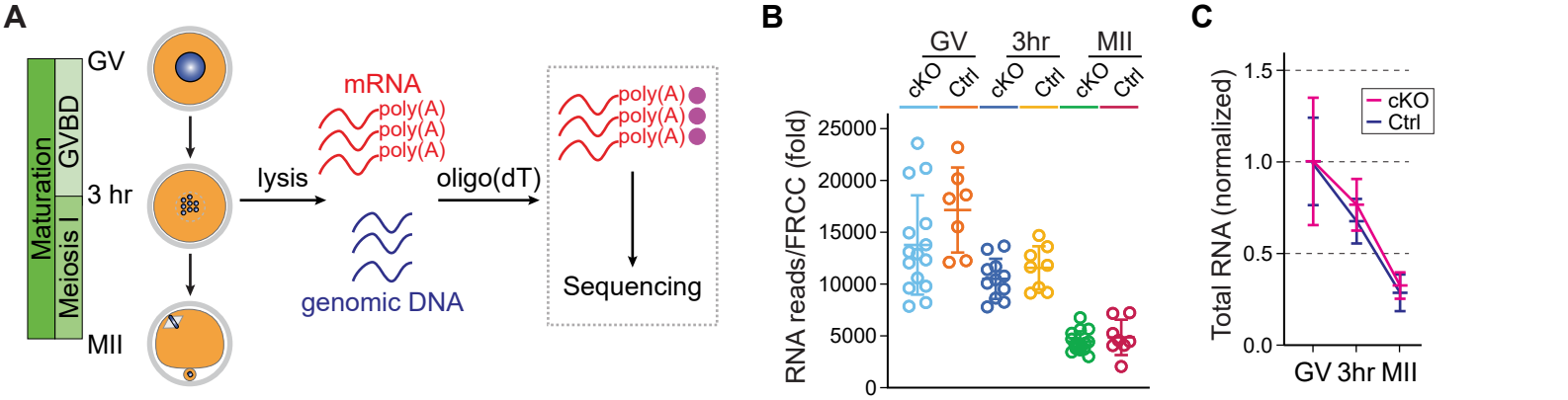

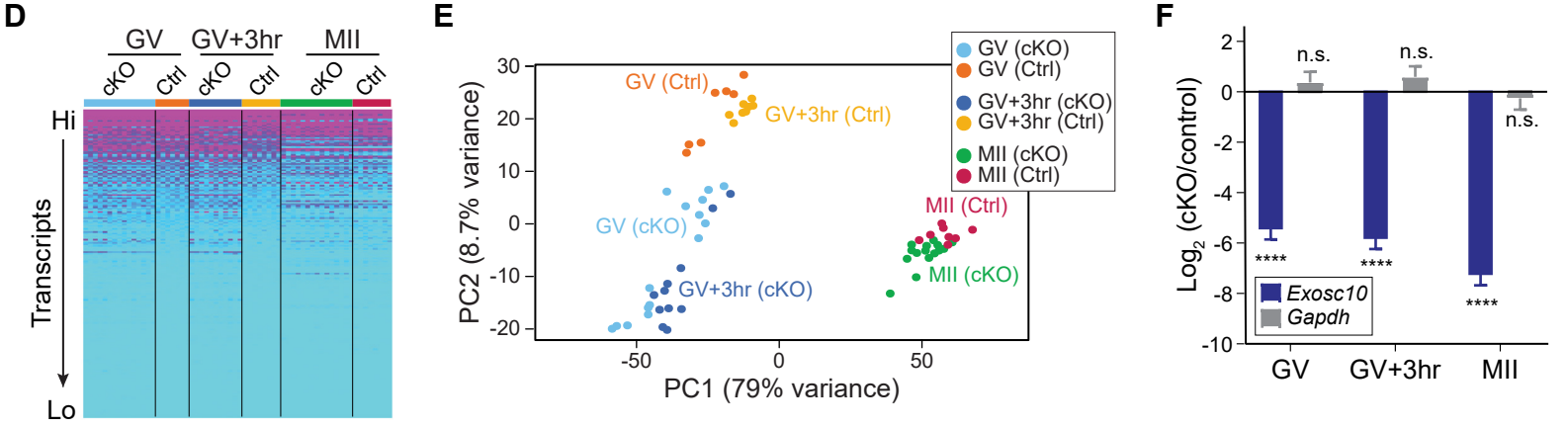

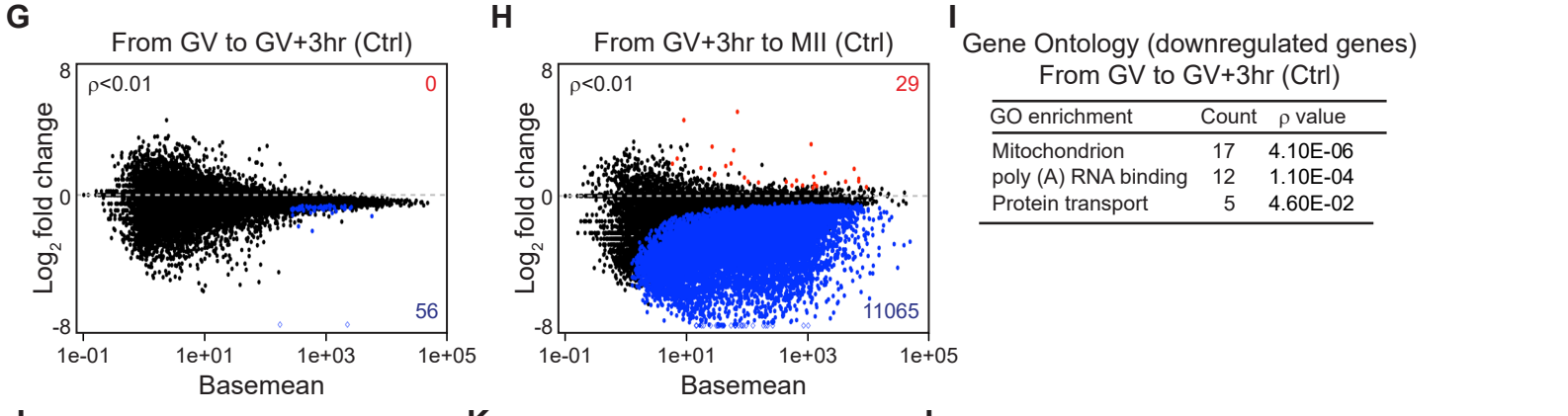

I

Gene Ontology (downregulated genes)
From GV to GV+3hr (Ctrl)

GO enrichment	Count	ρ value
Mitochondrion	17	4.10E-06
poly (A) RNA binding	12	1.10E-04
Protein transport	5	4.60E-02

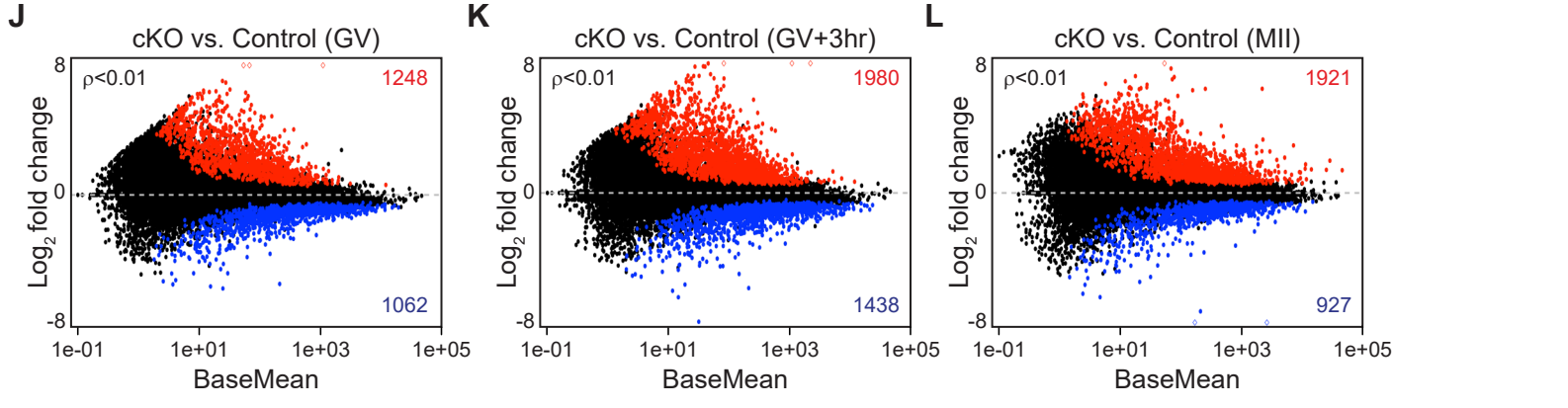

M

Gene Ontology (upregulated genes)

GO enrichment	GV		GV+3hr	
	Count	ρ value	Count	ρ value
Transcription	131	1.38E-09	190	1.35E-09
RNA-binding	46	9.16E-05	96	3.92E-09
Protein transport	46	3.50E-05	58	0.002571
Endoplasmic reticulum	53	0.048552	111	0.003365
Endosome	29	0.016971	13	0.00391
Meiotic cell cycle	10	0.02398	14	0.009362

Figure 3

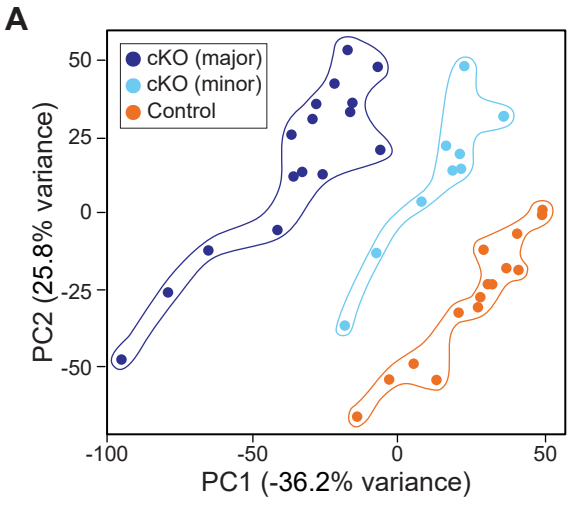

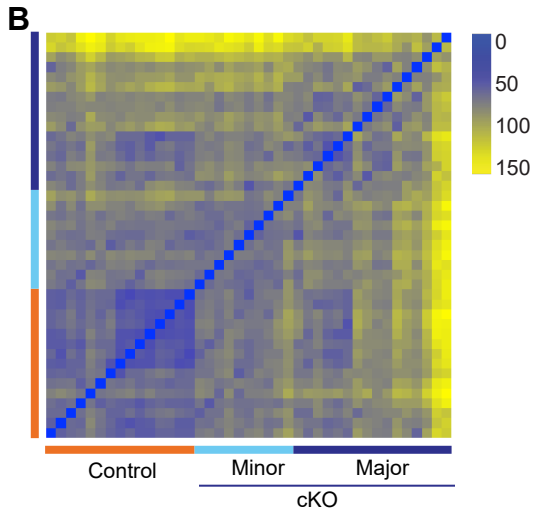

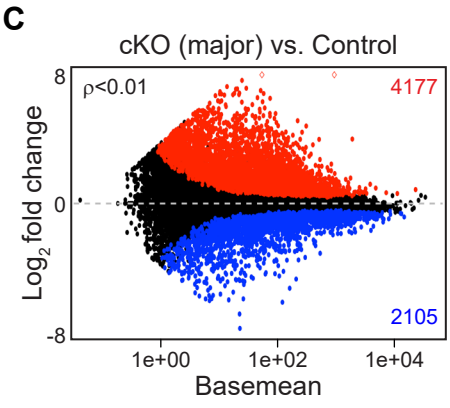

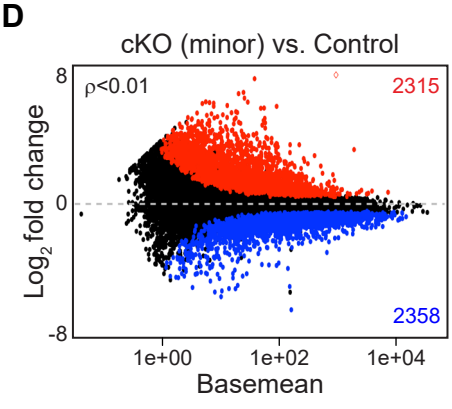

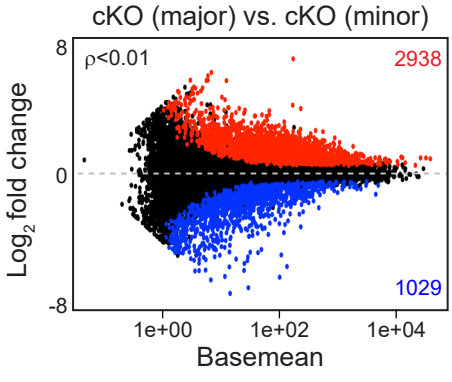

F

Gene ontology of upregulated genes
cKO (major) vs cKO (minor)

GO enrichment	Count	Pvalue
Transcription	270	7.4E-25
Mitochondrion	118	7.5E-5
Protein transport	71	2.3E-3
Cell cycle	62	4.2E-2
Endoplasmic reticulum stress	8	2.8E-2

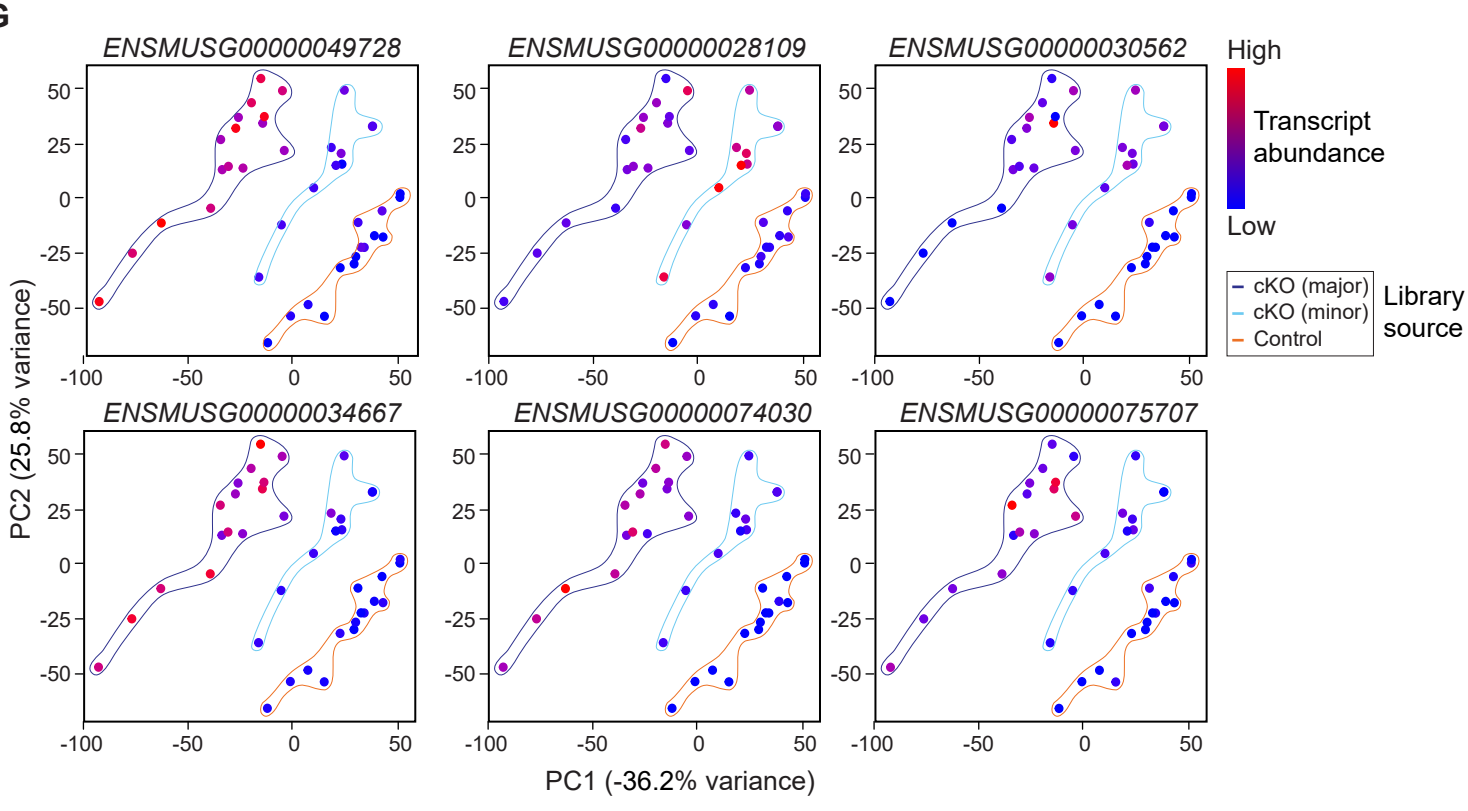

Figure 4

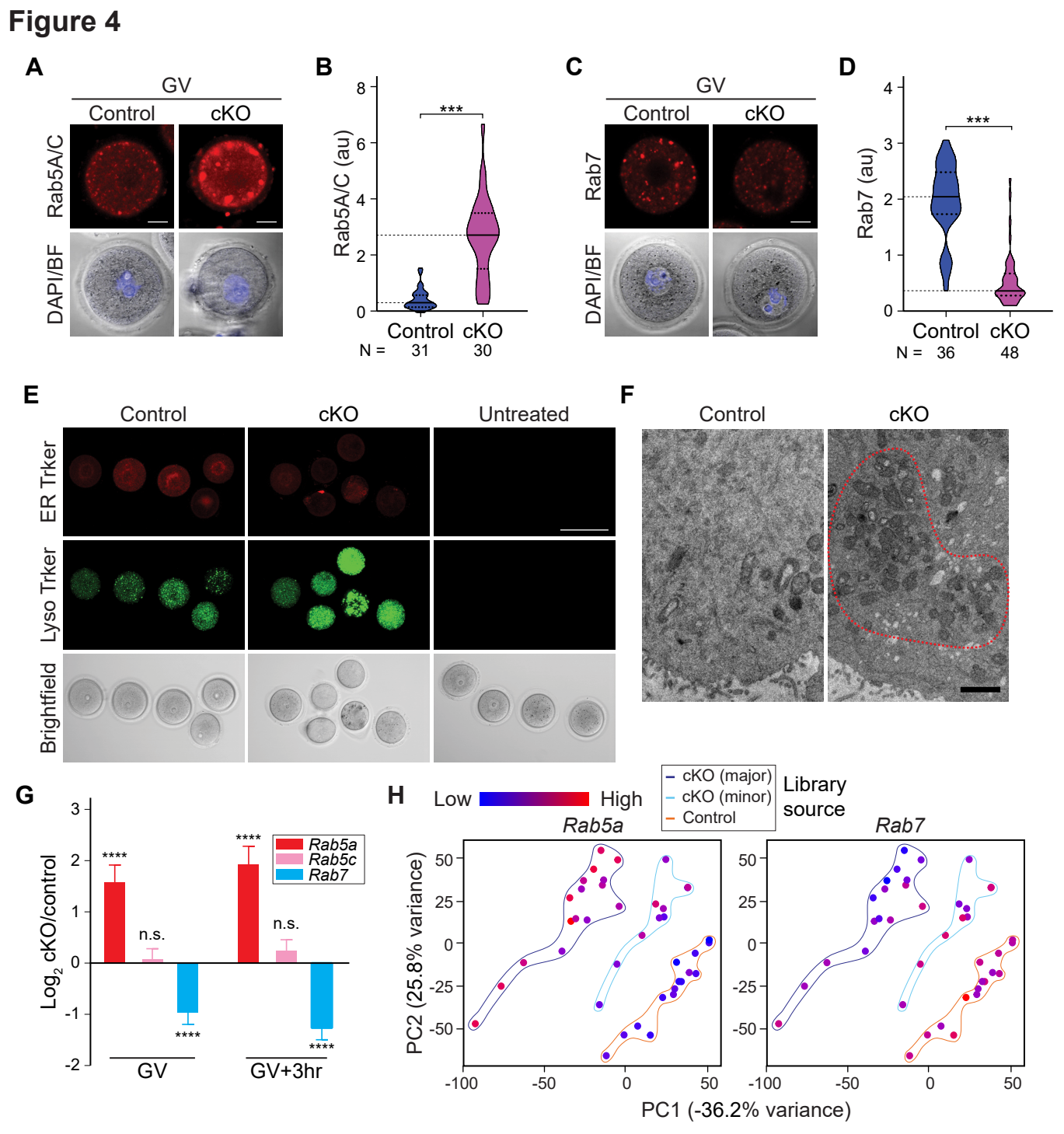
A
GV
Control
cKO
Rab5A/C
DAPI/BF
B
Rab5A/C (au)
***
Control
cKO
N =
31
30
C
GV
Control
cKO
Rab7
DAPI/BF
D
Rab7 (au)
***
Control
cKO
N =
36
48
E
Control
cKO
Untreated
ER Trker
Lyso Trker
Brightfield
F
Control
cKO
G
Log2 cKO/control
Rab5a
Rab5c
Rab7
****
n.s.
GV
GV+3hr
H
Low
High
cKO (major)
cKO (minor)
Control
Library source
Rab5a
Rab7
PC2 (25.8% variance)
PC1 (-36.2% variance)

Figure 5

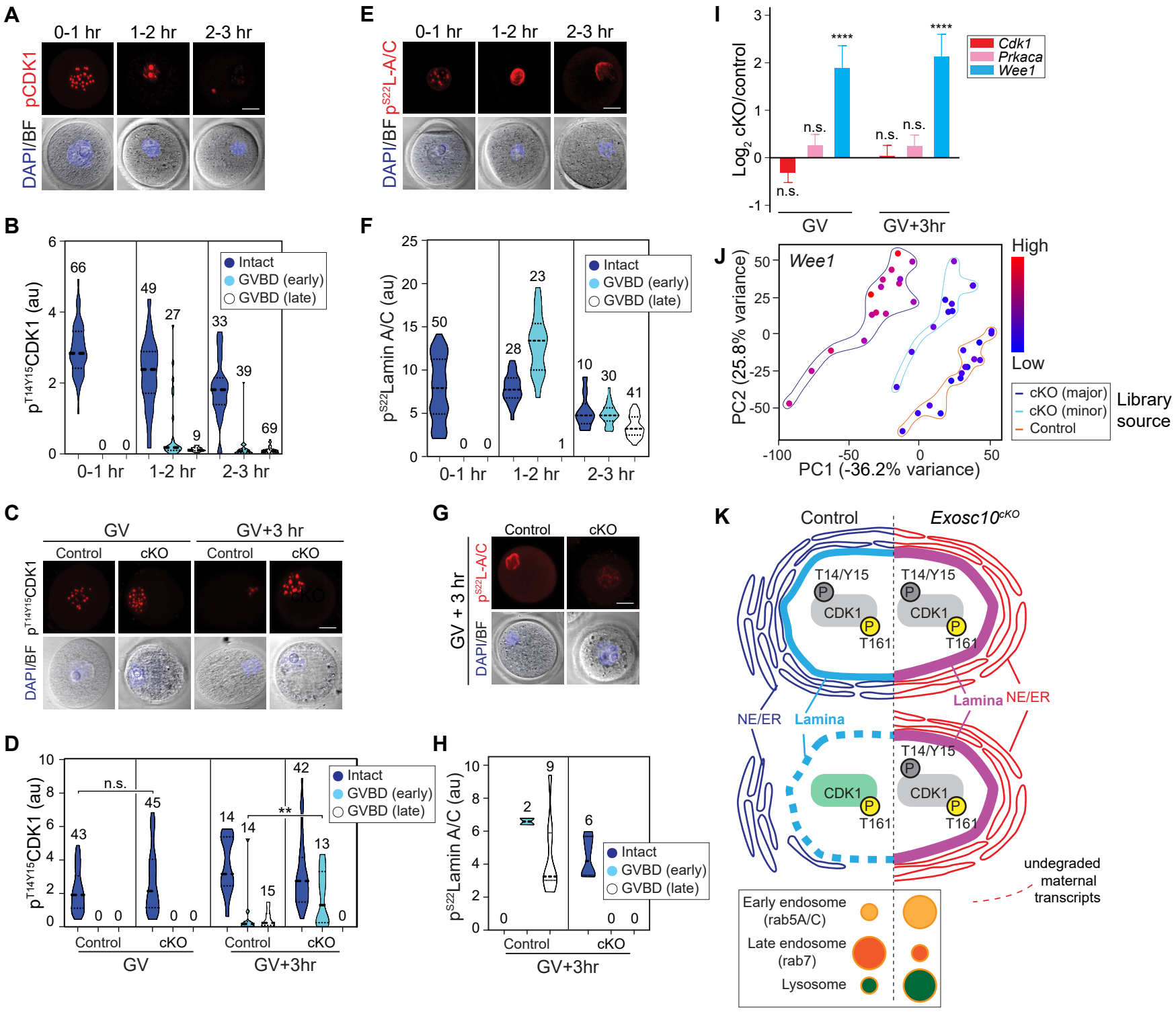
A
0-1 hr
1-2 hr
2-3 hr
pCDK1
DAPI/BF
E
pS22L-A/C
B
pT14Y15CDK1 (au)
Intact
GVBD (early)
GVBD (late)
F
pS22Lamin A/C (au)
I
Log2 cKO/control
Cdk1
Prkaca
Wee1
n.s.
****
GV
GV+3hr
J
Wee1
PC2 (25.8% variance)
PC1 (-36.2% variance)
High
Low
cKO (major)
cKO (minor)
Control
Library source
C
GV
GV+3 hr
Control
cKO
pT14Y15CDK1
DAPI/BF
G
GV + 3 hr
pS22L-A/C
D
n.s.
**
H
K
Exosc10cKO
T14/Y15
CDK1
T161
NE/ER
Lamina
undegraded maternal transcripts
Early endosome (rab5A/C)
Late endosome (rab7)
Lysosome